Chemical Science

ROYAL SOCIETY OF CHEMISTRY

EDGE ARTICLE

View Article Online
View Journal | View Issue

Check for updates

Cite this: *Chem. Sci.*, 2025, **16**, 8082

All publication charges for this article have been paid for by the Royal Society of Chemistry

Received 6th February 2025
Accepted 21st March 2025

DOI: 10.1039/d5sc00944h

rsc.li/chemical-science

Open Access Article. Published on 08 April 2025. Downloaded on 1/13/2026 11:30:04 PM. This article is licensed under a Creative Commons Attribution-NonCommercial 3.0 Unported Licence.

Unraveling microenvironment modification in an atomically dispersed bimetallic FeCu catalyst in the oxygen reduction reaction†

Lingmin Wu,[a] Yinghua Wang,[a] Chunfeng Shao,[b] Fanfei Sun,*[c] Liming Wang *[a] and Baitao Li *[a]

The important effect of microstructure in Fe–Cu bimetallic catalysts on the mechanism of the oxygen reduction reaction (ORR) was theoretically and experimentally investigated. Three types of Fe sites regulated by Cu were constructed: Fe clusters modified with Cu–N_4, Fe–Cu dimers, and isolated Fe/Cu single atoms. A theoretical study revealed that although copper could reduce the d-band center of Fe, the Fe–Cu dimer displayed unique attributes. Notably, the dimer increased the energy of *π antibonding orbitals combined with Fe^{2+}/Fe^{3+}-3d and *OH-2p, accelerated *OH removal and produced the lowest predicted overpotential (0.48 V). Three catalysts featuring the above models were experimentally embedded on porous nitrogen-doped carbon. FeCu-NC-2 with Fe–Cu dimers exhibited the most positive half-wave potentials of 0.904 V in alkaline and 0.720 V in neutral solutions. A Zn–air battery and a microbial fuel cell equipped with FeCu-NC-2 as the cathodic catalyst produced stable and high power densities of 568.6 mW cm^{-2} and 2467 mW m^{-2}, respectively.

1. Introduction

The development of renewable energy, such as fuel cells and metal–air batteries, is imperative in tackling the pressing energy crisis and environmental issues.[1–3] However, the inefficient oxygen reduction reaction (ORR) at the cathode limits their practical utilization.[4–6] Although Pt-based catalysts have significantly enhanced the ORR,[7] their prohibitive cost and poor stability continue to impede their widespread adoption.[8,9] Fe-based catalysts are considered as promising alternatives to precious Pt-based counterparts, owing to the unfilled d-orbitals of Fe that facilitate the ORR.[10,11] Unlike bulk catalysts such as Fe_3C or Fe particles, which expose only a small fraction of surface atoms,[12] Fe clusters,[13] Fe dual atoms,[14,15] and single-atomic Fe–N_4 catalysts with maximum atom utilization efficiency have garnered significant attention for their potential to enhance ORR performance.[16,17]

The intrinsic activity of an atomically dispersed Fe-based catalyst hardly achieved the desired ORR activity due to its strong adsorption of *OH intermediate.[18,19] Introducing secondary elements to disrupt the electronic structure of the Fe atom is an effective strategy to control the adsorption mentioned above.[20–23] A number of dual-atomic Fe–Cu–NC catalysts with different Fe–Cu bonding configurations have been reported. In the first model, the Fe atom is directly bonded with the Cu atom with an Fe–Cu distance of ~2.5 Å (model I).[24,25] In the second model, Fe and Cu single atoms are arbitrarily dispersed with an Fe–Cu distance longer than 5.0 Å (model II).[26] These two models demonstrated an improvement in the electronic configuration of active sites as well as ORR performance, compared to a single-atomic Fe–N_4 catalyst. In the third model, Fe clusters are functionalized by an adjacent Cu–N_4 single-atom site (model III), and the catalysts possess both high-density active Fe clusters and secondary Cu metal,[27] where the Cu–N_4 site adjusts the electronic structure of the Fe cluster to reduce the reaction free energy of *O_2 toward *OOH.[28] In the above three models, the active sites determined by theoretical studies are Fe rather than Cu sites, while Cu acts as a modulator.[24,29,30] In many publications, each study typically reported only one or two of the above structures. Nevertheless, the ORR performance varies greatly with synthesis procedure, operating, and measurement parameters. It is very difficult to determine which type of microstructure is the most effective for ORR performance; yet, this is a question that electrochemists have always sought to clarify. Theoretically and experimentally, constructing catalysts with the aforementioned three structures and

[a]Guangdong Provincial Key Laboratory of Fuel Cell Technology, School of Chemistry and Chemical Engineering, South China University of Technology, Guangzhou, 510640, China. E-mail: btli@scut.edu.cn; wanglm@scut.edu.cn

[b]Anhui Province Key Laboratory of Pollutant Sensitive Materials and Environmental Remediation, Department of Materials Science and Engineering, Huaibei Normal University, Huaibei, 235000, China

[c]Shanghai Synchrotron Radiation Facility, Shanghai Advanced Research Institute, Chinese Academy of Sciences, Shanghai, 201204, China. E-mail: sunfanfei@sinap.ac.cn

† Electronic supplementary information (ESI) available. See DOI: https://doi.org/10.1039/d5sc00944h

© 2025 The Author(s). Published by the Royal Society of Chemistry

Open Access Article. Published on 08 April 2025. Downloaded on 1/13/2026 11:30:04 PM.
This article is licensed under a Creative Commons Attribution-NonCommercial 3.0 Unported Licence.

weighing up their pros and cons in ORR performance are crucial and necessary for the bottom-up designing of catalysts with superior performance.

Here, models embedded with Cu–N_4-modified Fe clusters (Fe_5–CuN_4), Fe–Cu dimers, and isolated Fe and Cu single atoms (FeCu-isolated) were constructed. Density functional theory (DFT) calculations expounded that the d-band centers of all the three models decreased after incorporating Cu, but the Fe–Cu dimer exhibited the lowest d-band center (−1.40 eV) and the highest *π antibonding orbitals of Fe^{2+}/Fe^{3+}-3d and *OH-2p, which benefited the removal of *OH and resulted in the lowest predicted overpotential (0.48 V). Guided by the theoretical results, three catalysts (FeCu-NC-*x*) with the aforementioned three structures were synthesized by adjusting only the molar ratio of Cu/Fe, while ensuring that all other conditions were identical. Aberration-corrected high angle annular dark field (HAADF)-STEM and X-ray adsorption spectroscopy (XAS) analysis revealed that the above three types of active site were successfully embedded on porous nitrogen-doped carbon. Notably, FeCu-NC-2 with Fe–Cu dimer sites exhibited superior ORR performance, outperforming FeCu-NC-1 and FeCu-NC-3, which have different structures. It also showed great potential for applications in both Zn–air batteries (ZABs) and microbial fuel cells (MFCs).

2. Results and discussion

DFT calculations were performed on three models: FeCu-dimer, Fe_5–CuN_4 and FeCu-isolated (Fig. S1†). The $*O_2$, *OOH, *O and *OH intermediates adsorbed on the catalysts are depicted in Fig. S2.† For the FeCu-dimer model, at $U = 0$ V, each elementary step was exothermic (Fig. 1a). However, at $U = 1.23$ V, the protonation of *O to *OH exhibited the highest endothermicity, with a ΔG_3 of 0.48 eV (Table S1†), indicating that this step is the rate-determining step; and the corresponding overpotential was 0.48 V. Similarly, the overpotentials of Fe_5–CuN_4 and FeCu-isolated were 0.65 and 0.84 V, respectively (Table S1†). These values were all lower than those of FeN_4 (0.93 V) and CuN_3 (1.14 V) single atoms (Fig. S3 and S4†), suggesting the unique synergistic interaction between Fe and Cu atoms. This was because stronger oxygen adsorption on FeN_4 made the dissociation of *OH challenging,[31] while weak oxygen adsorption for CuN_3 made oxygen adsorption difficult.[32] The linear relationship between *OH and $*O_2$ adsorption energies (named $E_{ads,*OH}$ and $E_{ads,*O_2}$) (Fig. S5†) further suggested that, while the incorporation of Cu weakens the interaction between oxygen and FeN_4, it also accelerates the removal of *OH, resulting in a lower overpotential in the Fe–Cu bimetallic catalyst. The d-band center of Fe atoms provides insight into this interaction: generally, a lower d-band center corresponds to weaker adsorption.[33,34] FeCu-dimer exhibited the lowest d-band center at −1.40 eV, followed by Fe_5–CuN_4 (−1.05 eV), with FeCu-isolated showing the smallest reduction at −0.72 eV (Fig. 1b). These values were all lower than that of FeN_4 (−0.66 eV) (Fig. S6†). The relationship between d-band center and overpotential (blue line in Fig. 1f) emphasized the decisive role of the introduced Cu atoms in alleviating adsorption. A decrease

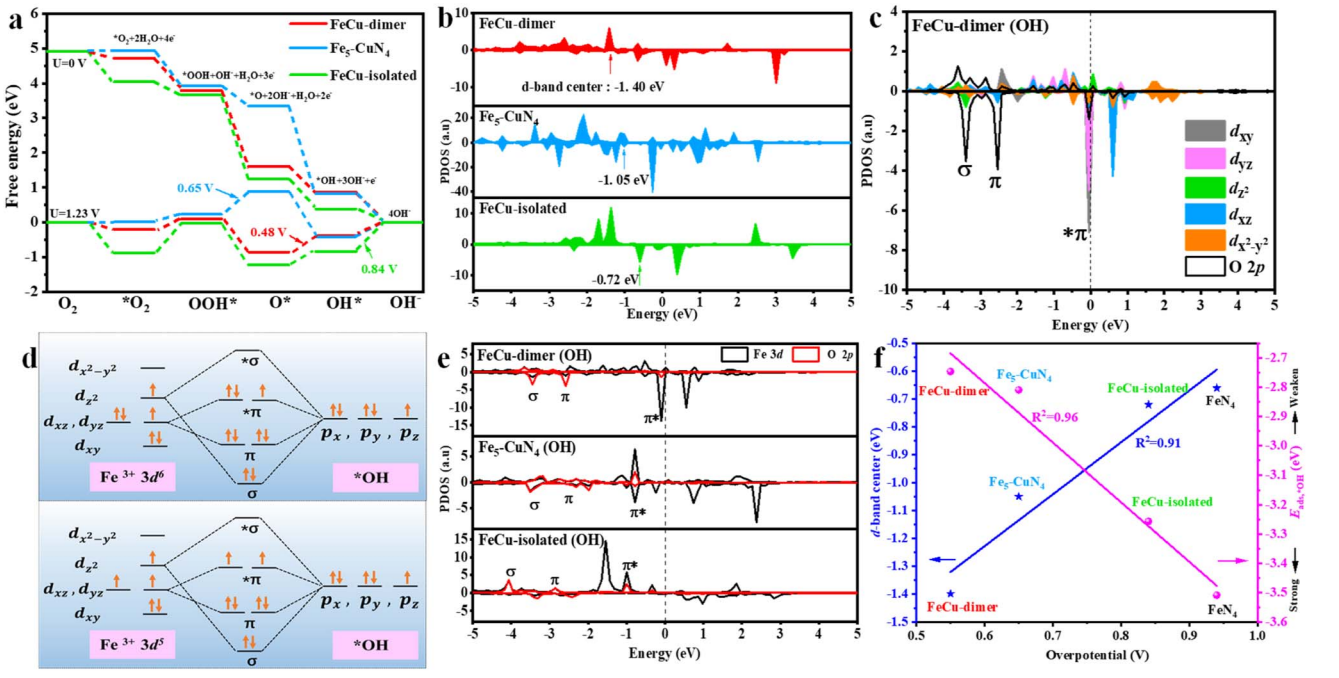

Fig. 1 Free energy diagram (a); computed projected density of states (PDOS) before (b) and after *OH adsorption (e); PDOS (c) and orbital interaction (d) depicting overlap of Fe-3d and O-2p in FeCu-dimer; linear scaling relationship between the d-band center and E_{ads*OH} *versus* predicted overpotential (f). FeCu-dimer (OH), Fe_5–CuN_4(OH) and FeCu-isolated (OH) in (c) and (e) indicate the three models after *OH adsorption.

Open Access Article. Published on 08 April 2025. Downloaded on 1/13/2026 11:30:04 PM. This article is licensed under a Creative Commons Attribution-NonCommercial 3.0 Unported Licence.

in the d-band center modulated the adsorption of intermediates, which was vital for enhancing electrocatalytic ORR activity.

Furthermore, the changes in d-sub-orbitals before and after *OH modification were explored. In the pristine FeCu-dimer, the unfilled $d_{x^2-y^2}$ orbital had the highest energy, above the Fermi level (Fig. S7a†). Meanwhile, the d_{xz} and d_{z^2} orbitals were half-filled, and the d_{xz} and d_{xy} orbitals were fully filled.[35] After *OH adsorbed on the Fe active sites in FeCu-dimer, the d_{z^2} orbitals overlapped with the p_z orbital in *OH, forming a σ bond. The d_{xz} and d_{yz} orbitals individually overlapped with p_x and p_y orbitals in *OH, forming two π bonding orbitals and two *π antibonding orbitals (Fig. 1c and d).[36,37] Similar bonding interactions, σ bonds, π bonds, and *π bonds, were observed in Fe_5–CuN_4 (Fig. S7b†) and FeCu-isolated (Fig. S7c†). A higher energy for the *π antibonding orbitals meant weakened interaction between *OH and active sites.[27] The *π orbital energy followed the trend FeCu-dimer > Fe_5–CuN_4 > FeCu-isolated (Fig. 1e), indicating that FeCu-dimer had a significant advantage in *OH removal; this is in agreement with a lower $E_{ads,*OH}$ for FeCu-dimer (Fig. S5†). Furthermore, $E_{ads,*OH}$ and the predicted overpotential (the pink line in Fig. 1f) exhibited a linear relationship, suggesting that reducing $E_{ads,*OH}$ on Fe sites directly enhances the ORR performance. Overall, the FeCu-dimer was predicted to show the best ORR performance.

Furthermore, the corresponding catalysts (FeCu-NC-*x*) were synthesized by adjusting the molar ratio of Cu/Fe from 1 to 3 with SiO_2 as a porosity-inducing template (Fig. 2a). Both FeCu-NC-*x* and Cu-NC catalysts exhibited tightly packed pore structures (Fig. 2b and S8a–e†). However, a more constricted aperture was observed in the Fe–NC catalyst (Fig. S8d†), due to the easy aggregation of a number of Fe ions (2.81 wt%) (Table S2†) after the removal of SiO_2.[38] All the catalysts exhibited typical type IV curves with H3 hysteresis (Fig. S9†), indicating the presence of numerous mesopores.[39,40] Their surface areas were all greater than 900 $m^2\ g^{-1}$ (Table S2†). Furthermore, the TEM (Fig. S8i†) and energy-dispersive X-ray spectra (EDS) (Fig. S8k†) revealed obvious iron particles in Fe–NC, but no metal particles could be detected in FeCu-NC-*x* (Fig. S8f–h†) or Cu–NC (Fig. S8j†). The XRD pattern of Fe–NC showed the existence of iron carbide, but no related species were observed in the FeCu-NC-*x* or Cu–NC catalysts (Fig. S10a†), showing that the addition of Cu prevented the accumulation of iron.[41] The aberration-corrected HAADF-STEM showed the presence of clusters (~0.8 nm, red circles) and single atoms in FeCu-NC-1 (Fig. 2g). According to the ICP results (Table S2†), these clusters were identified as Fe clusters. The Fe clusters became less abundant with the decrease in Fe dosage. A significant presence of atomic pairs (red circles) and single atoms was observed in FeCu-NC-2

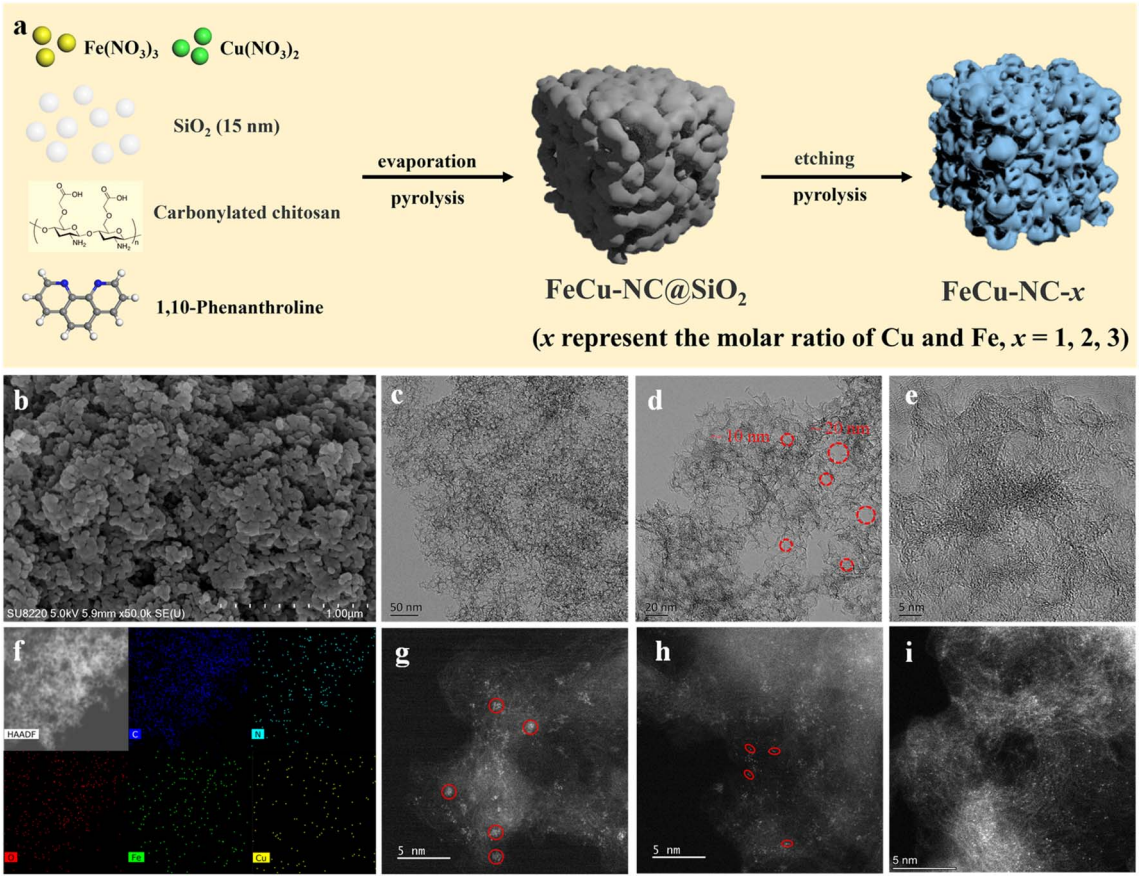

Fig. 2 Synthesis procedure of FeCu-NC-*x* (a); SEM images (b), TEM images (c)–(e), HAADF-STEM image and corresponding elemental distribution (f) of FeCu-NC-2; aberration-corrected HAADF-STEM images of FeCu-NC-1 (g), FeCu-NC-2 (h) and FeCu-NC-3 (i).

© 2025 The Author(s). Published by the Royal Society of Chemistry

Open Access Article. Published on 08 April 2025. Downloaded on 1/13/2026 11:30:04 PM.
This article is licensed under a Creative Commons Attribution-NonCommercial 3.0 Unported Licence.

(Fig. 2h, S10b and c†). No clusters were observed in FeCu-NC-3 (Fig. 2i), and the quantity of single atoms was lower than that in FeCu-NC-2, due to the reduction in Fe loading. Thus, the microenvironment of bimetallic Fe and Cu can be achieved by adjusting the Cu/Fe molar ratio.

The surface electronic structures of Fe and Cu atoms were analyzed *via* X-ray photoelectron spectroscopy (XPS). The Fe 2p spectra showed peaks at 710.8/723.6 eV and 713.0/726.0 eV, corresponding to ferrous (Fe^{2+}) and ferric (Fe^{3+}) states,[42] respectively (Fig. S11†).[43] Fe–NC displayed a higher Fe^{2+}/Fe^{3+} ratio (2.18) (Table S3†) than that of the FeCu-NC-*x* catalysts, suggesting electron transfer from Fe to Cu. The ratio increased from 1.50 to 1.83 as the Fe content increased from FeCu-NC-3 to FeCu-NC-1.This observation can be further confirmed by the Cu 2p spectra (Fig. S12†). Compared to the lower ratio of Cu^{+}/Cu^{2+} in Cu–NC (0.72), FeCu-NC-*x* exhibited higher values (>0.80), further supporting electron transfer from Fe to Cu. The high-resolution N 1s spectra could be deconvoluted into four peaks at 398.3, 399.5, 401.0, and 404.0 eV, attributed to pyridinic N, metal-N, graphitic N, and oxidized N, respectively (Fig. S13†).[44] Among these, pyridinic N,[45] metal-N[46,47] and graphitic N[48] were regarded as active N species favorable to ORR performance, and Fe–N was more active than Cu–N.[49,50] Thus, FeCu-NC-2 exhibited the highest concentration of active N species (Table S4†), suggesting the substantial potential for ORR activity in Fe-NC-2.

The coordination environments of Fe and Cu atoms in the FeCu-NC-*x* catalysts were investigated by XAS. Fe K-edge XANES of FeCu-NC-*x* were set between FeO and Fe_2O_3, revealing the presence of Fe^{2+} and Fe^{3+} in the bimetallic catalyst (Fig. 3a).[51] The average oxidation state of Fe increased from FeCu-NC-1 (2.35) to FeCu-NC-3 (2.57) (Fig. 3b),[24] reflecting a decrease in the Fe^{2+}/Fe^{3+} ratio, which agreed well with the result from XPS (Table S3†). Accordingly, the average oxidation state of Cu decreased from FeCu-NC-1 (1.49) to FeCu-NC-3 (1.12) (Fig. 3d and e),[52,53] further indicating electron transfer from Fe to Cu atoms. Furthermore, the Fourier transform (FT)-EXAFS of the Fe K-edge revealed a primary peak located at ~1.41 Å (Fig. 3c), corresponding to the Fe–N path or Fe–O scattering. Additionally, FeCu-NC-1 displayed a weak shoulder peak at 2.27 Å (Fig. 4a), suggesting the existence of a Fe-metal path.[54] No such peak was detected in FeCu-NC-2 (Fig. 4b) or FeCu-NC-3 (Fig. 4c), where Fe atoms were more dispersed. Similarly, the Cu K-edge FT-EXAFS plots showed a Cu–O or Cu–N peak at ~1.47 Å (Fig. 3f),[55] with FeCu-NC-2 showing a secondary peak at 2.38 Å (Fig. 4e), indicating Cu-metal bonding.[56] The EXAFS fitting revealed that the coordination number of Fe–N in FeCu-NC-1 was 3.02 and that of Cu–N was 3.98 (Table S5†). As no obvious Cu-metal path was detected in the Cu K-edge of FeCu-NC-1 in *R* space (Fig. 4d), the Fe-metal path in the Fe K-edge of FeCu-NC-1 was ascribed to Fe–Fe scattering. While FeCu-NC-2 presented small amounts of Fe–Cu dimers and abundant $Fe–N_4$ single atoms (Fig. 4b and e), FeCu-NC-3 showed highly dispersed Fe single atoms and Cu single atoms, each coordinated with three nitrogen atoms (Fig. 4c, f, and Table S5†). The Cu–NC catalyst was well-fitted with Cu–N scattering (Fig. S14 and Table S5†) with a coordination number 4.02. Moreover, the Fe K-edge wavelet-transformed (WT) EXAFS of FeCu-NC-1 and FeCu-NC-2 both exhibited two intensity maxima: one at $k \approx 4.50$ $Å^{-1}$ belonging to Fe–N and another at 6.65 $Å^{-1}$ in FeCu-NC-1, attributed to the Fe–Fe path (Fig. 4g); the peak at 6.90 $Å^{-1}$ in

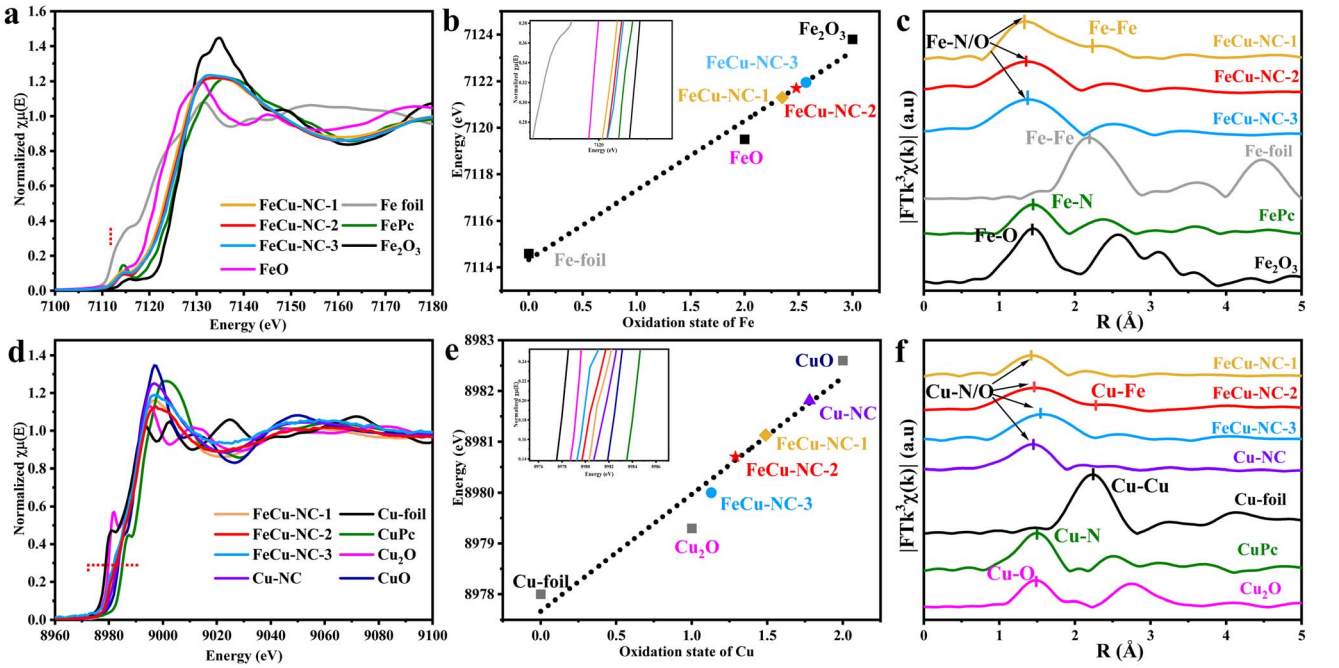

Fig. 3 X-ray absorption spectroscopy data of FeCu-NC-*x*. XANES spectra of the Fe K-edge (a) and Cu K-edge (d); fitted oxidation state of the Fe K-edge (b) and Cu K-edge (e) based on the XANES spectra of the first derivative; k^3-weighted Fourier transform (FT) EXAFS spectra of the Fe K-edge (c) and Cu K-edge (f).

Open Access Article. Published on 08 April 2025. Downloaded on 1/13/2026 11:30:04 PM.
This article is licensed under a Creative Commons Attribution-NonCommercial 3.0 Unported Licence.

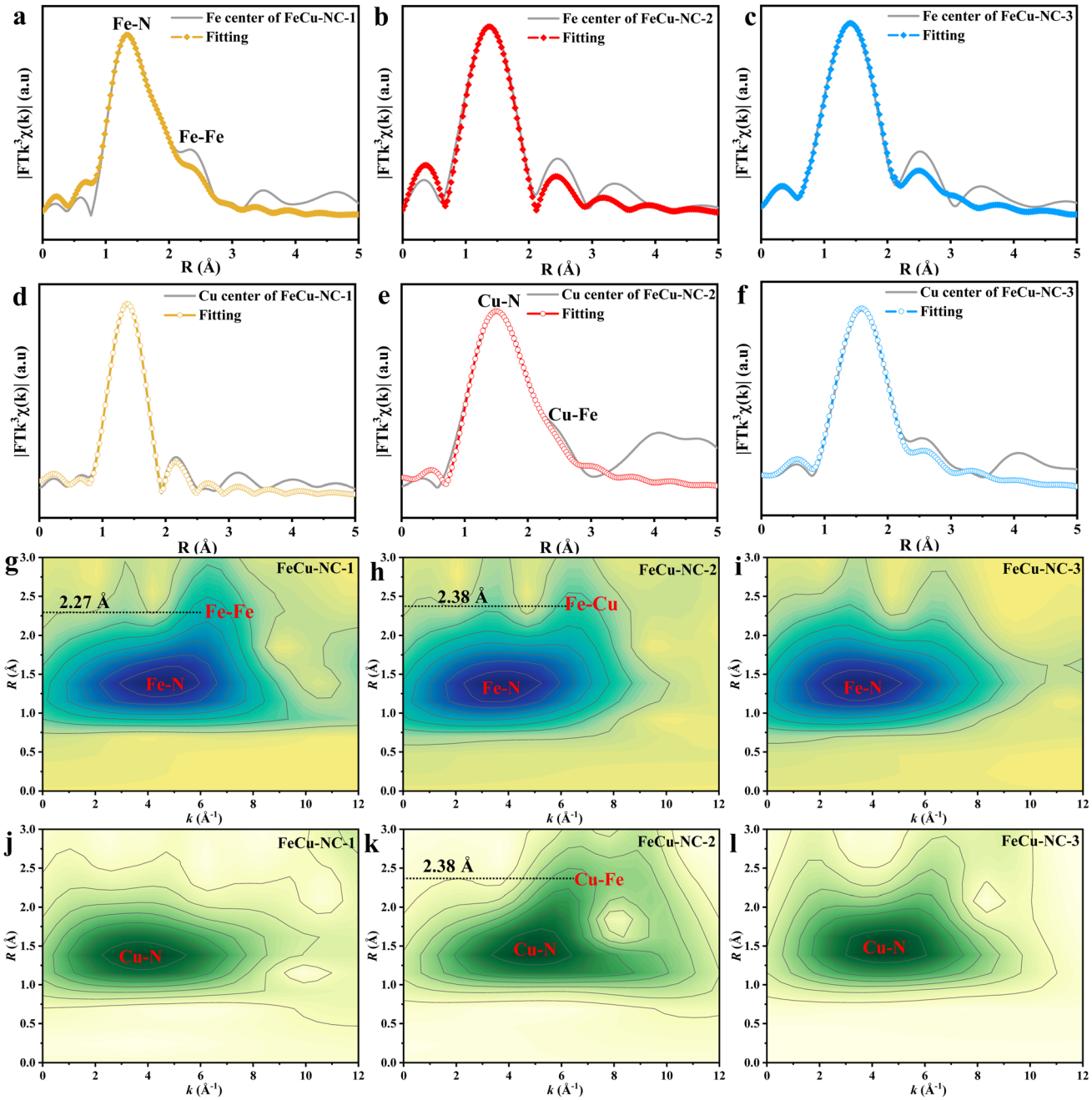

Fig. 4 EXAFS fitting spectra of the Fe K-edge and Cu K-edge in *R* space for FeCu-NC-1 (a and d), FeCu-NC-2 (b and e) and FeCu-NC-3 (c and f), and wavelet-transform contour plots of the k^3-weighted EXAFS data of Fe K-edge (g–i) and Cu K-edge (j–l).

FeCu-NC-2 was ascribed to the Fe–Cu path (Fig. 4h). Only one intensity maximum at 3.61 $Å^{-1}$ (Fig. 4i) was detected in FeCu-NC-3. The Cu K-edge WT-EXAFS of FeCu-NC-2 alone showed two intensity maxima at $k \approx 4.97$ $Å^{-1}$ and 6.95 $Å^{-1}$, which were related to the Cu–N and Cu–Fe paths (Fig. 4k), respectively and were different from those of Cu foil (Fig. S15d†) and Cu_2O (Fig. S15f†). All the other catalysts displayed one intensity maximum at 4.0 $Å^{-1}$ (Fig. 4j, l and S14b†) assignable to the Cu–N path (Fig. S15e†).

The electrocatalytic activity of the FeCu-NC-*x* catalysts toward ORR was investigated in an O_2-saturated 0.1 M KOH solution. FeCu-NC-2 demonstrated the most positive half-wave potential ($E_{1/2}$) of 0.904 V and onset potential (E_{onset}) of 1.012 V, exceeding those of FeCu-NC-1 (0.891 V, 1.022 V) and FeCu-NC-3 (0.877 V, 0.982 V) (Fig. 5a and b), highlighting the significant advantage of Fe–Cu dimers in the FeCu-NC-2 catalyst over the Fe clusters in Fe-NC-1 and individual Fe/Cu single atoms in FeCu-NC-3. Meanwhile, the $E_{1/2}$ values of the FeCu-NC-*x* catalysts surpassed those of the monometallic catalysts, Fe–NC (0.856 V) and Cu–NC (0.836 V), indicating the special interactions between Fe and Cu atoms. Additionally, different batches of FeCu-NC-2 were tested (Fig. S16†), for which the LSV

© 2025 The Author(s). Published by the Royal Society of Chemistry

Open Access Article. Published on 08 April 2025. Downloaded on 1/13/2026 11:30:04 PM.
This article is licensed under a Creative Commons Attribution-NonCommercial 3.0 Unported Licence.

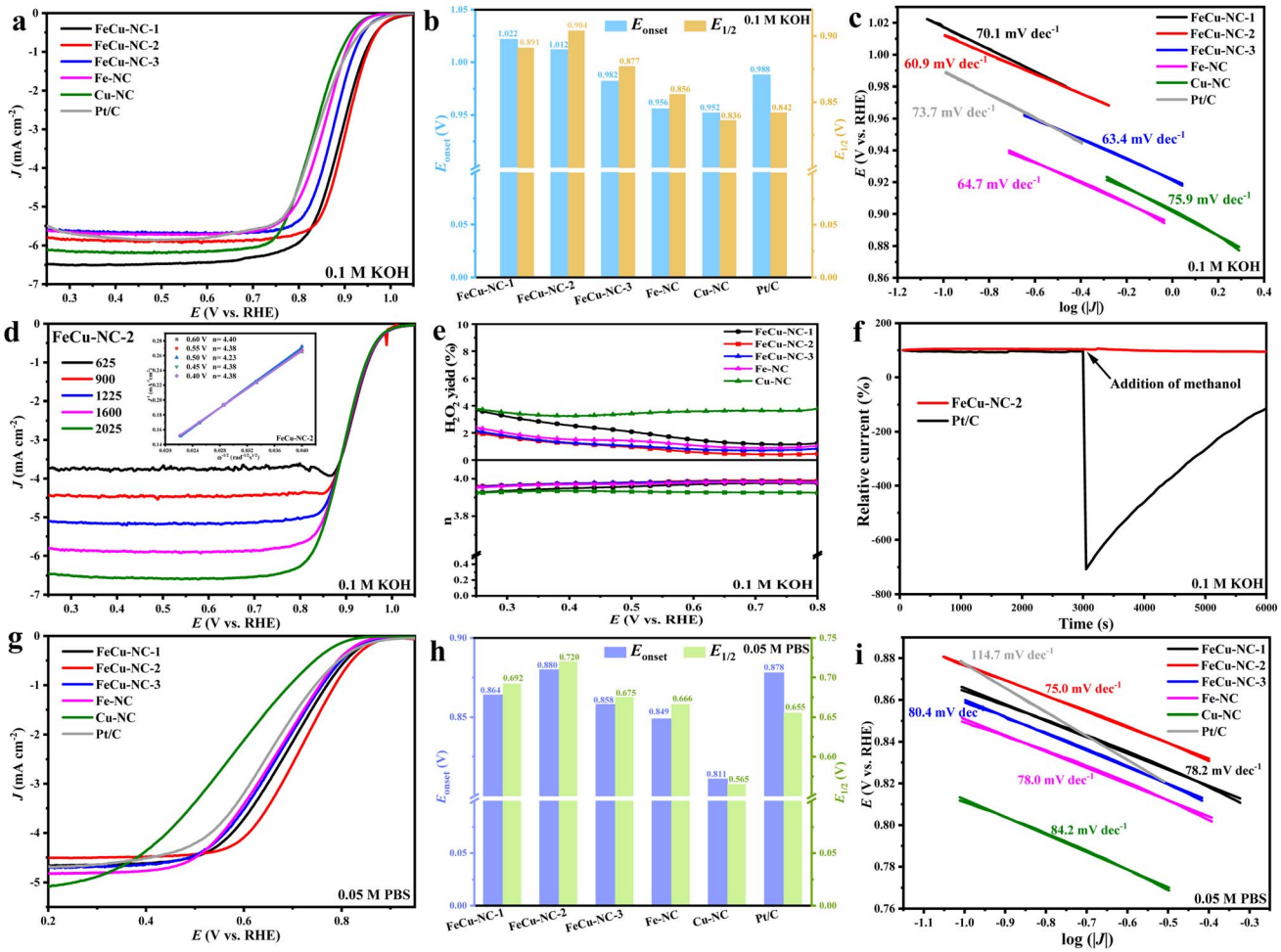

Fig. 5 Electrocatalytic performance of FeCu-NC-*x*, Fe–NC, Cu–NC and Pt/C catalysts. LSV curves at 1600 rpm (a), the value of onset potential (E_{onset}) and half-wave potential ($E_{1/2}$) (b), Tafel slope (c) and peroxide yields and electron transfer number (e) in 0.1 M KOH solution; LSV curves at 1600 rpm (g), the value of E_{onset} and $E_{1/2}$ (h) and Tafel slope (i) in 0.05 M PBS solution; LSV curves of FeCu-NC-2 at different rotation speeds from 625 to 2025 rpm (d) and the corresponding electron transfer number (e) and methanol crossover effect test of FeCu-NC-2 (f) in 0.1 M KOH.

curves almost overlapped and the $E_{1/2}$ varied from 0.900 V to 0.904 V, with a low standard deviation of 0.002, suggesting good reproducibility of the synthesis process. Furthermore, FeCu-NC-2 displayed the smallest Tafel slope of 60.9 mV dec^{-1} (Fig. 5c), indicating its outstanding kinetics.[57,58] The electrochemically active surface areas (ECSAs) were evaluated by double-layer capacitance (C_{dl}) (Fig. S17†), with FeCu-NC-2 showing the highest C_{dl} (21.4 mF cm^{-2}), in line with the trend of ORR activity. Koutecky–Levich (K–L) plots demonstrated that the electron transfer numbers (n) of all the catalysts (Fig. 5d, S18 and S19†) were comparable to that of Pt/C (4.10), indicating that the catalysts followed a four-electron pathway. RRDE measurements showed a similar result, in which all the catalysts had a peroxide yield of less than 5%, with n close to 4.0, confirming the four-electron pathway (Fig. 5e).

The stability of FeCu-NC-2 was assessed using the normalized current–time (i–t) method. It maintained 84.9% of its initial current after 45 000 s, comparable to Pt/C (81.3%) (Fig. S20a†). The corresponding $E_{1/2}$ of FeCu-NC-2 decreased by only 20 mV, while Pt/C exhibited a decrease of 26 mV (Fig. S20b and S20c†), demonstrating its excellent stability. After 10 000 consecutive cycles in accelerated durability testing (ADT), FeCu-NC-2 showed a small change in $E_{1/2}$ (7 mV) (Fig. S21a†) and retained its porous structure (Fig. S22a†) without any metal aggregation (Fig. S22b†), suggesting its stability in terms of both structure and activity. Additionally, methanol tolerance tests (Fig. 5f) showed that FeCu-NC-2 exhibited no significant change in current. Overall, FeCu-NC-2 demonstrated excellent ORR activity and stability in 0.1 M KOH, which was comparable to similar types of previously reported state-of-the-art non-precious-metal catalysts (Table S6†).

The ORR activity of the prepared catalysts were also investigated in 0.05 M PBS solution (Fig. 5g and h), where FeCu-NC-2 displayed excellent activity with an outstanding $E_{1/2}$ of 0.720 V and E_{onset} of 0.880 V. This value surpassed those of other reported FeCu bimetallic catalysts (Table S7†) and was better than those of FeCu-NC-1, FeCu-NC-3, and Pt/C. The Tafel slopes of the synthesized catalysts were similar (75–85 mV dec^{-1}) but inferior to that of Pt/C (114.7 mV dec^{-1}) (Fig. 5i). Furthermore, the K–L equation and RRDE results (Fig. S23†) also suggested

Open Access Article. Published on 08 April 2025. Downloaded on 1/13/2026 11:30:04 PM. This article is licensed under a Creative Commons Attribution-NonCommercial 3.0 Unported Licence.

that FeCu-NC-2 abided by a four-electron pathway. Interestingly, better long-time stability was detected in FeCu-NC-2, which retained 90.2% of the initial current (Fig. S20d†) and exhibited only 19 mV damping in $E_{1/2}$ (Fig. S20e†) after 45 000 s. In contrast, the current of Pt/C decreased to nearly half (58.1%) of its initial value (Fig. S20d and S20f†). After 10 000 consecutive cycles in ADT, FeCu-NC-2 also retained its good durability, with unnoticeable variation (3 mV) for $E_{1/2}$ (Fig. S21b†).

Zn–air batteries (ZABs) were constructed using FeCu-NC-2 and Pt/C as cathodic catalysts (Fig. S24a†). FeCu-NC-2-ZAB exhibited an open-circuit voltage (OCV) of 1.57 V, 120 mV higher than that of Pt/C-ZAB (Fig. S24b†). The voltage for FeCu-NC-2-ZAB plateaued at a higher value than that for Pt/C-ZAB across various current densities (Fig. S24c†). The specific capacity of FeCu-NC-2-ZAB was 736.2 mA h g_{Zn}^{-1}, with a corresponding energy density of 994.2 W h kg_{Zn}^{-1} at 10 mA cm^{-2}, surpassing those of Pt/C-ZAB (678.3 mA h g_{Zn}^{-1}, 858.0 W h kg_{Zn}^{-1}) (Fig. S24d†). It also achieved a peak power density of 568.6 mW cm^{-2}, approximately triple that of Pt/C-ZAB (207.9 mW cm^{-2}) (Fig. S24e†) and surpassed those of most reported catalysts (Table S6†). Furthermore, FeCu-NC-2-ZAB displayed remarkable durability, maintaining 97.4% of its initial voltage over 14 h of discharge (Fig. S24f†), compared to 94.3% for Pt/C-ZAB. The round-trip efficiency of FeCu-NC-2-ZAB was 67.7%, 64.9%, and 64.3% at 8, 20, and 36 h, respectively (Fig. S25†), highlighting its superior stability compared to Pt/C-ZAB. Two FeCu-NC-2-ZAB cells successfully powered LED bulbs (inset in Fig. S24f†). Overall, FeCu-NC-2 exhibited great potential in practical ZAB applications.

Similarly, in view of the excellent ORR performance of FeCu-NC-2 in neutral solution, its potential application in microbial fuel cells (MFCs) was investigated. As illustrated in Fig. S24g,† MFCs can generate electricity while degrading organic matter from sewage, where anaerobic bacteria oxidize organic material at the anode, releasing electrons to the cathode for oxygen reduction.[59,60] FeCu-NC-2-MFC showed superior OCV (0.72 V) and achieved an impressive power density of 2467 ± 56 mW m^{-2}, surpassing that of Pt/C-MFC (1689 ± 94 mW m^{-2}) (Fig. S24h†). Additionally, FeCu-NC-2-MFC exhibited minimal voltage decay (2.6%) over 550 h (Fig. S24i†), indicating remarkable long-term stability. With respect to wastewater treatment, FeCu-NC-2-MFC achieved higher chemical oxygen demand (COD) removal (85.3%) and coulombic efficiency (6.98%) than Pt/C-MFC (83.0% and 6.86%) (Fig. S26b†), suggesting its efficiency in converting organic matter into electrical current. The comparable performance of FeCu-NC-2 to previously reported Fe/Cu catalysts (Table S7†) further confirmed its great advantages in MFC applications.

3. Conclusion

A theoretical study revealed that the lowest predicted overpotential for Fe–Cu dimers was due to the downshifted d-band center, which led to an increase in energy of *π antibonding orbitals combined with Fe^{2+}/Fe^{3+}-3d and *OH-2p, and a significant decrease in adsorption energy with *OH and $*O_2$ intermediates. In an experimental study, the microenvironment of porous FeCu-NC catalysts was tailored by adjusting the molar ratio of Cu/Fe and three catalysts— Cu–N_4 modified Fe clusters (Fe_5–CuN_4), Fe–Cu dimers, and isolated Fe and Cu single atoms (FeCu-isolated)—were obtained. FeCu-NC-2 with a Fe–Cu dimer structure showed outstanding ORR performance in both alkaline and neutral solutions, with the highest $E_{1/2}$ (0.904 V, 0.720 V) and favorable Tafel slope (60.9 mV dec^{-1}, 75.0 mV dec^{-1}). When applied as a cathodic catalyst in ZAB and MFC, FeCu-NC-2 demonstrated admirable power density (568.6 mW cm^{-2} for ZAB, 2467 ± 56 mW m^{-2} for MFC) and excellent stability. Overall, the Fe–Cu dimer could be a more promising microstructure for future energy conversion devices. This research makes a valuable contribution to high-performance ORR catalysts. The promising results of the FeCu-NC-2 catalyst suggest that further research into its potential high performance under an acid electrolyte could pave the way for its large-scale application in polymer electrolyte membrane fuel cells and proton exchange membrane fuel cells. Additionally, exploring other bimetallic sources, such as, FeCo, FeNi, and FeMn, could broaden the feasibility of this synthesis approach.

Data availability

The data supporting this article have been included as part of the ESI.†

Author contributions

Lingmin Wu: writing – original draft, methodology, investigation, data curation, conceptualization. Yinghua Wang: methodology, investigation. Chunfeng Shao: methodology, investigation. Fanfei Sun: methodology, resources, data curation. Liming Wang: supervision, methodology, validation, funding acquisition. Baitao Li: writing – review & editing, validation, supervision, resources, project administration, funding acquisition.

Conflicts of interest

There are no conflicts to declare.

Acknowledgements

This research was supported by the National Natural Science Foundation of China (21872056, U2032152) and Natural Science Foundation of Guangdong Province (2023A1515011249, 2021A1515010149). The authors thank BL20U of Shanghai Synchrotron Radiation Facilities (SSRF) for providing the beam time and thank Dr Fanfei Sun and Dr Jingyuan Ma.

References

1 H. Liu, F. Yu, K. Wu, G. Xu, C. Wu, H. K. Liu and S. X. Dou, Recent progress on Fe-based single/dual-atom catalysts for Zn–air batteries, *Small*, 2022, **18**, e2106635.
2 S. Liu, A. Wang, Y. Liu, W. Zhou, H. Wen, H. Zhang, K. Sun, S. Li, J. Zhou and Y. Wang, Catalytically active carbon for

© 2025 The Author(s). Published by the Royal Society of Chemistry

Open Access Article. Published on 08 April 2025. Downloaded on 1/13/2026 11:30:04 PM. This article is licensed under a Creative Commons Attribution-NonCommercial 3.0 Unported Licence.

oxygen reduction reaction in energy conversion: recent advances and future perspectives, *Adv. Sci.*, 2024, **11**, 2308040.

3 S. Ding, L. He, L. Fang, Y. Zhu, T. Li, Z. Lyu, D. Du, Y. Lin and J. C. Li, Carbon-nanotube-bridging strategy for integrating single Fe atoms and NiCo nanoparticles in a bifunctional oxygen electrocatalyst toward high-efficiency and long-life rechargeable zinc–air batteries, *Adv. Energy Mater.*, 2022, **12**, 2202984.

4 C. Fu, X. Qi, L. Zhao, T. Yang, Q. Xue, Z. Zhu, P. Xiong, J. Jiang, X. An and H. Chen, Synergistic cooperation between atomically dispersed Zn and Fe on porous nitrogen-doped carbon for boosting oxygen reduction reaction, *Appl. Catal., B*, 2023, **335**, 122875.

5 A. Morozan, B. Jousselme and S. Palacin, Low-platinum and platinum-free catalysts for the oxygen reduction reaction at fuel cell cathodes, *Energy Environ. Sci.*, 2011, **4**, 1238–1254.

6 X. Tian, X. Lu, B. Xia and X. Lou, Advanced electrocatalysts for the oxygen reduction reaction in energy conversion technologies, *Joule*, 2020, **4**, 45–68.

7 L. Zhang, T. Zeng, L. Zheng, Y. Wang, W. Yuan, M. Niu, C. Guo, D. Cao and C. Li, Epitaxial growth of Pt–Pd bimetallic heterostructures for the oxygen reduction reaction, *Adv. Powder Mater.*, 2023, **2**, 100131.

8 N. Shang, C. Wang, X. Zhang, S. Gao, S. Zhang, T. Meng, J. Wang, H. Wang, C. Du and T. Shen, Atomically dispersed iron on nitrogen-decorated carbon for high-performance oxygen reduction and zinc–air batteries, *Chem. Eng. J.*, 2021, **426**, 127345.

9 M. CostadeOliveira, A. D'Epifanio, H. Ohnuki and B. Mecheri, Platinum group metal-free catalysts for oxygen reduction reaction: applications in microbial fuel cells, *Catalysts*, 2020, **10**, 475.

10 X. Wang, Z. Kang, D. Wang, Y. Zhao, X. Xiang, H. Shang and B. Zhang, Electronic structure regulation of the Fe-based single-atom catalysts for oxygen electrocatalysis, *Nano Energy*, 2024, **121**, 109268.

11 U. Martinez, S. KominiBabu, E. Holby, H. Chung, X. Yin and P. Zelenay, Progress in the development of Fe-based PGM-free electrocatalysts for the oxygen reduction reaction, *Adv. Mater.*, 2019, **31**, 1806545.

12 Y. Yan, H. Cheng, Z. Qu, R. Yu, F. Liu, Q. Ma, S. Zhao, H. Hu, Y. Cheng, C. Yang, Z. Li, X. Wang, S. Hao, Y. Chen and M. Liu, Recent progress on the synthesis and oxygen reduction applications of Fe-based single-atom and double-atom catalysts, *J. Mater. Chem. A*, 2021, **9**, 19489–19507.

13 L. Yuan, B. Liu, L. Shen, Y. Dai, Q. Li, C. Liu, W. Gong, X. Sui and Z. Wang, d-orbital electron delocalization realized by axial Fe_4C atomic clusters delivers high-performance Fe–N–C catalysts for oxygen reduction reaction, *Adv. Mater.*, 2023, **35**, 2305945.

14 Y. Xu, W. Li, L. Chen, W. Li, W. Feng and X. Qiu, Regulating the N-coordination structure of Fe–Fe dual sites as the electrocatalyst for the O2 reduction reaction in metal–air batteries, *Inorg. Chem.*, 2023, **62**, 5253–5261.

15 K. Leng, J. Zhang, Y. Wang, D. Li, L. Bai, J. Shi, X. Li, L. Zheng, J. Bai and Y. Qu, Interfacial cladding engineering suppresses atomic thermal migration to fabricate well-defined dual-atom electrocatalysts, *Adv. Funct. Mater.*, 2022, **32**, 2205637.

16 T. He, A. Santiago, Y. Kong, M. Ahsan, R. Luque, A. Du and H. Pan, Atomically dispersed heteronuclear dual-atom catalysts: a new rising star in atomic catalysis, *Small*, 2022, **18**, e2106091.

17 Q. Wang, Y. Yang, F. Sun, G. Chen, J. Wang, L. Peng, W. T. Chen, L. Shang, J. Zhao and D. Sun, Molten NaCl-assisted synthesis of porous Fe–N–C electrocatalysts with a high density of catalytically accessible FeN_4 active sites and outstanding oxygen reduction reaction performance, *Adv. Energy Mater.*, 2021, **11**, 2100219.

18 L. Gong, H. Zhang, Y. Wang, E. Luo, K. Li, L. Gao, Y. Wang, Z. Wu, Z. Jin and J. Ge, Bridge bonded oxygen ligands between approximated FeN_4 sites confer catalysts with high ORR performance, *Angew. Chem., Int. Ed.*, 2020, **132**, 14027–14032.

19 Z. Chen, X. Su, J. Ding, N. Yang, W. Zuo, Q. He, Z. Wei, Q. Zhang, J. Huang and Y. Zhai, Boosting oxygen reduction reaction with Fe and Se dual-atom sites supported by nitrogen-doped porous carbon, *Appl. Catal., B*, 2022, **308**, 121206.

20 D. Yu, Y. Ma, F. Hu, C. C. Lin, L. Li, H. Y. Chen, X. Han and S. Peng, Dual-sites coordination engineering of single atom catalysts for flexible metal–air batteries, *Adv. Energy Mater.*, 2021, **11**, 2101242.

21 S. Huang, Z. Qiao, P. Sun, K. Qiao, K. Pei, L. Yang, H. Xu, S. Wang, Y. Huang and Y. Yan, The strain induced synergistic catalysis of FeN_4 and MnN_3 dual-site catalysts for oxygen reduction in proton-/anion-exchange membrane fuel cells, *Appl. Catal., B*, 2022, **317**, 121770.

22 L. Wu, Y. Chen, C. Shao, L. Wang and B. Li, Engineering synergetic Fe–Co atomic pairs anchored on porous carbon for enhanced oxygen reduction reaction, *Adv. Funct. Mater.*, 2024, **34**, 2408257.

23 S. Ding, J. A. Barr, Q. Shi, Y. Zeng, P. Tieu, Z. Lyu, L. Fang, T. Li, X. Pan and S. P. Beckman, Engineering atomic single metal–FeN_4Cl sites with enhanced oxygen-reduction activity for high-performance proton exchange membrane fuel cells, *ACS Nano*, 2022, **16**, 15165–15174.

24 M. Xu, L. Zhang, X. Liang, H. Xiao, H. Zhuang, F. Zhang, T. Zhang, P. Han, W. Dai, F. Gao, J. Zhang, L. Zheng and Q. Gao, Dual-atom $Fe(II,III)N_2(\mu_2\text{-}N)_2Cu(I,II)N$ moieties anchored on porous N-doped carbon driving high-efficiency oxygen reduction reaction, *Appl. Catal., B*, 2024, **349**, 123866.

25 Y. Zhang, S. Zhang, H. Huang, X. Liu, B. Li, Y. Lee, X. Wang, Y. Bai, M. Sun, Y. Wu, S. Gong, X. Liu, Z. Zhuang, T. Tan and Z. Niu, General synthesis of a diatomic catalyst library *via* a macrocyclic precursor-mediated approach, *J. Am. Chem. Soc.*, 2023, **145**, 4819–4827.

26 H. Yang, T. Zhang, X. Chi, X. Yu, J. Chen, J. Chen, C. Li, S. Tan, Q. He, X. Wang and L. Wang, Promoting oxygen reduction *via* coordination environment modulation

Open Access Article. Published on 08 April 2025. Downloaded on 1/13/2026 11:30:04 PM. This article is licensed under a Creative Commons Attribution-NonCommercial 3.0 Unported Licence.

through secondary metal-atom incorporation, *J. Mater. Chem. A*, 2022, **10**, 19626–19634.

27 C. Qi, H. Yang, Z. Sun, H. Wang, N. Xu, G. Zhu, L. Wang, W. Jiang, X. Yu, X. Li, Q. Xiao, P. Qiu and W. Luo, Modulating electronic structures of iron clusters through orbital rehybridization by adjacent single copper sites for efficient oxygen reduction, *Angew. Chem., Int. Ed. Engl.*, 2023, **62**, e202308344.

28 S. Wu, S. Jiang, S. Liu, X. Tan, N. Chen, J. Luo, S. Mushrif, K. Cadien and Z. Li, Single Cu–N_4 sites enable atomic Fe clusters with high-performance oxygen reduction reactions, *Energy Environ. Sci.*, 2023, **16**, 3576–3586.

29 K. Srinivas, Z. Chen, A. Chen, H. Huang, C. Yang, F. Wang, M. Zhu and Y. Chen, Dual single-atom sites coupled with graphene-encapsulated core–shell Fe–Cu nanoalloy for boosting the oxygen reduction reaction, *J. Mater. Chem. A*, 2024, **12**, 28398–28413.

30 L. Wu, Y. Wang, C. Shao, L. Wang and B. Li, Copper single atom-modulated functionalization of iron clusters on a porous carbon nanosheet for the oxygen reduction reaction, *J. Mater. Chem. A*, 2025, **13**, 5974–5986.

31 S. Zhang, Y. Qin, S. Ding and Y. Su, A DFT study on the activity origin of Fe–N–C sites for oxygen reduction reaction, *ChemPhysChem*, 2022, **23**, e202200165.

32 H. Wu, X. Xu, J. Wu, J. Zhai, F. Wu, Y. Li, S. Jiang, J. Zhang, H. Li and Y. Gao, Atomic engineering modulates oxygen reduction of hollow carbon matrix confined single metal-nitrogen sites for zinc–air batteries, *Small*, 2023, **19**, 2301327.

33 C. Deng, Y. Su, F. Li, W. Shen, Z. Chen and Q. Tang, Understanding activity origin for the oxygen reduction reaction on bi-atom catalysts by DFT studies and machine-learning, *J. Mater. Chem. A*, 2020, **8**, 24563–24571.

34 X. Li, S. Duan, E. Sharman, Y. Zhao, L. Yang, Z. Zhuo, P. Cui, J. Jiang and Y. Luo, Exceeding the volcano relationship in oxygen reduction/evolution reactions using single-atom-based catalysts with dual-active-sites, *J. Mater. Chem. A*, 2020, **8**, 10193–10198.

35 Y. Dai, B. Liu, Z. Zhang, P. Guo, C. Liu, Y. Zhang, L. Zhao and Z. Wang, Tailoring the d-orbital splitting manner of single atomic sites for enhanced oxygen reduction, *Adv. Mater.*, 2023, **35**, 2210757.

36 D. Xue, Y. Yuan, Y. Yu, S. Xu, Y. Wei, J. Zhang, H. Guo, M. Shao and J.-N. Zhang, Spin occupancy regulation of the Pt d-orbital for a robust low-Pt catalyst towards oxygen reduction, *Nat. Commun.*, 2024, **15**, 5990.

37 J. Zhang, F. Li, W. Liu, Q. Wang, X. Li, S.-F. Hung, H. Yang and B. Liu, Modulating spin of atomic manganese center for high-performance oxygen reduction reaction, *Angew. Chem., Int. Ed.*, 2024, **63**, e202412245.

38 Q. Ma, H. Jin, J. Zhu, Z. Li, H. Xu, B. Liu, Z. Zhang, J. Ma and S. Mu, Stabilizing Fe–N–C catalysts as model for oxygen reduction reaction, *Adv. Sci.*, 2021, **8**, 2102209.

39 C. Shao, S. Zhuang, H. Zhang, Q. Jiang, X. Xu, J. Ye, B. Li and X. Wang, Enhancement of mass transport for oxygen reduction reaction using petal-like porous Fe–NC nanosheet, *Small*, 2021, **17**, 2006178.

40 J. Du, A. Chen, S. Hou and J. Guan, CNT modified by mesoporous carbon anchored by Ni nanoparticles for CO_2 electrochemical reduction, *Carbon Energy*, 2022, **4**, 1274–1284.

41 K. Zhang, Y. Zhang, Q. Zhang, Z. Liang, L. Gu, W. Guo, B. Zhu, S. Guo and R. Zou, Metal-organic framework-derived Fe/Cu-substituted Co nanoparticles embedded in CNTs-grafted carbon polyhedron for Zn–air batteries, *Carbon Energy*, 2020, **2**, 283–293.

42 M. Yang, J. Xie, Z. Lin, B. Dong, Y. Chen, X. Ma, M. Wen, Y. Zhou, L. Wang and Y. Chai, N-doped FeP nanorods derived from Fe-MOFs as bifunctional electrocatalysts for overall water splitting, *Appl. Surf. Sci.*, 2020, **507**, 145096.

43 Y. Zang, H. Zhang, X. Zhang, R. Liu, S. Liu, G. Wang, Y. Zhang and H. Zhao, Fe/Fe_2O_3 nanoparticles anchored on Fe-N-doped carbon nanosheets as bifunctional oxygen electrocatalysts for rechargeable zinc–air batteries, *Nano Res.*, 2016, **9**, 2123–2137.

44 L. Xu, Y. Tian, D. Deng, H. Li, D. Zhang, J. Qian, S. Wang, J. Zhang, H. Li and S. Sun, Cu nanoclusters/FeN_4 amorphous composites with dual active sites in N-doped graphene for high-performance Zn–air batteries, *ACS Appl. Mater. Interfaces*, 2020, **12**, 31340–31350.

45 D. Guo, R. Shibuya, C. Akiba, S. Saji, T. Kondo and J. Nakamura, Active sites of nitrogen-doped carbon materials for oxygen reduction reaction clarified using model catalysts, *Science*, 2016, **351**, 361–365.

46 K. Singh, F. Razmjooei and J. Yu, Active sites and factors influencing them for efficient oxygen reduction reaction in metal-N coordinated pyrolyzed and non-pyrolyzed catalysts: a review, *J. Mater. Chem. A*, 2017, **5**, 20095–20119.

47 Y. Wang, H. Su, Y. He, L. Li, S. Zhu, H. Shen, P. Xie, X. Fu, G. Zhou and C. Feng, Advanced electrocatalysts with single-metal-atom active sites, *Chem. Rev.*, 2020, **120**, 12217–12314.

48 R. Sidik, A. Anderson, N. Subramanian, S. Kumaraguru and B. Popov, O_2 reduction on graphite and nitrogen-doped graphite: experiment and theory, *J. Phys. Chem. B*, 2006, **110**, 1787–1793.

49 J. Li, J. Chen, H. Wan, J. Xiao, Y. Tang, M. Liu and H. Wang, Boosting oxygen reduction activity of Fe–NC by partial copper substitution to iron in Al–air batteries, *Appl. Catal., B*, 2019, **242**, 209–217.

50 C. Du, Y. Gao, H. Chen, P. Li, S. Zhu, J. Wang, Q. He and W. Chen, A Cu and Fe dual-atom nanozyme mimicking cytochrome c oxidase to boost the oxygen reduction reaction, *J. Mater. Chem. A*, 2020, **8**, 16994–17001.

51 C. Shao, L. Wu, Y. Wang, K. Qu, H. Chu, L. Sun, J. Ye, B. Li and X. Wang, An open superstructure of hydrangea-like carbon with highly accessible Fe-N_4 active sites for enhanced oxygen reduction reaction, *Chem. Eng. J.*, 2022, **429**, 132307.

52 G. Xing, M. Tong, P. Yu, L. Wang, G. Zhang, C. Tian and H. Fu, Reconstruction of highly dense Cu–N_4 active sites in electrocatalytic oxygen reduction characterized by operando synchrotron radiation, *Angew. Chem., Int. Ed.*, 2022, **61**, e202211098.

© 2025 The Author(s). Published by the Royal Society of Chemistry

Open Access Article. Published on 08 April 2025. Downloaded on 1/13/2026 11:30:04 PM.
This article is licensed under a Creative Commons Attribution-NonCommercial 3.0 Unported Licence.

53 J. Yang, W. Liu, M. Xu, X. Liu, H. Qi, L. Zhang, X. Yang, S. Niu, D. Zhou and Y. Liu, Dynamic behavior of single-atom catalysts in electrocatalysis: identification of Cu-N_3 as an active site for the oxygen reduction reaction, *J. Am. Chem. Soc.*, 2021, **143**, 14530–14539.

54 C. Shao, L. Wu, H. Zhang, Q. Jiang, X. Xu, Y. Wang, S. Zhuang, H. Chu, L. Sun and J. Ye, A versatile approach to boost oxygen reduction of Fe-N4 sites by controllably incorporating sulfur functionality, *Adv. Funct. Mater.*, 2021, **31**, 2100833.

55 G. Han, X. Zhang, W. Liu, Q. Zhang, Z. Wang, J. Cheng, T. Yao, L. Gu, C. Du and Y. Gao, Substrate strain tunes operando geometric distortion and oxygen reduction activity of CuN_2C_2 single-atom sites, *Nat. Commun.*, 2021, **12**, 6335.

56 S. Zhang, J. Wu, M. Zheng, X. Jin, Z. Shen, Z. Li, Y. Wang, Q. Wang, X. Wang and H. Wei, Fe/Cu diatomic catalysts for electrochemical nitrate reduction to ammonia, *Nat. Commun.*, 2023, **14**, 3634.

57 Z. Sun, H. Zhang, L. Cao, X. Liu, D. Wu, X. Shen, X. Zhang, Z. Chen, S. Ru and X. Zhu, Understanding synergistic catalysis on Cu-Se dual atom sites *via* operando X-ray absorption spectroscopy in oxygen reduction reaction, *Angew. Chem., Int. Ed.*, 2023, **135**, e202217719.

58 H. Yang, H. Huang, Q. Wang, L. Shang, T. Zhang and S. Wang, Fe, Cu dual-metal single atom catalyst on commercial carbon black for efficient oxygen reduction reaction, *J. Mater. Chem. A*, 2023, **11**, 6191–6197.

59 B. Li, Q. Li and X. Wang, Iron/iron carbide coupled with S, N co-doped porous carbon as effective oxygen reduction reaction catalyst for microbial fuel cells, *Environ. Res.*, 2023, **228**, 115808.

60 C. Shao, J. Hua, Q. Li, Y. Xia, L. Sun, L. Wang and B. Li, Near-range modulation of single-atomic Fe sites by simultaneously integrating heteroatom and nanocluster for efficient oxygen reduction, *Nano Energy*, 2024, **126**, 109668.